

The Energy Dependence of the Aperiodic Variability for Cygnus X-1, GX 339-4, GRS 1758-258 & 1E 1740.7-2942

D. Lin¹, I. A. Smith¹, M. Böttcher^{1,2}, & E. P. Liang¹

ABSTRACT

Using the data from the *Rossi X-ray Timing Explorer (RXTE)*, we report the different energy dependence of the variability of the four persistent hard X-ray sources in the low-hard state: Cygnus X-1, GX 339-4, GRS 1758-258 and 1E 1740.7-2942. Cygnus X-1 is found to have a flatter power density spectrum (PDS) shape at higher energies. The other three sources have energy independent PDS shapes. The energy dependence of the overall variability (the integrated rms amplitude) varies from source to source and from observation to observation. 1E 1740.7-2942, for example, has a variability generally increasing with energy while GX 339-4 has a decreasing variability. A general trend is found in the four sources that the integrated rms amplitude anti-correlates with the X-ray flux. We compare these distinct energy dependent behaviors with several emission models. None of the models can fully explain all the features that we have found.

Subject headings: accretion, accretion disks — black hole physics — stars: individual (Cygnus X-1, GX 339-4, GRS 1758-258, 1E 1740.7-2942) — X-rays: stars

1. Introduction

The galactic black-hole candidates (GBHCs) are known to exhibit rapid variability on time scales of hours down to milliseconds. This rapid aperiodic and quasiperiodic variability provides a diagnostic tool for understanding the nature of the high-energy emission in these objects (for reviews see van der Klis 1995; Cui 1998; Liang 1998). The power density spectrum (PDS) of the variation is one of the widely studied properties. Generally the PDS of GBHCs consists of a flat plateau at low frequencies (red noise) up to a break frequency f_1 and a power-law, typically $\propto f^{-1}$ for $f > f_1$. In several sources, a second break is observed at frequency f_2 , beyond which the PDS turns into a steeper power-law, typically $\propto f^{-\beta}$ with $1.5 \lesssim \beta \lesssim 2$. Hereafter, we will refer to this structure using a double broken power-law model (although it can generally be equally well

¹Department of Space Physics and Astronomy, Rice University, 6100 S. Main, Houston, TX 77005, USA. Email: lin@spacsun.rice.edu.

²Chandra Fellow.

described using two zero centered lorentzians). Superposed on the above shape some GBHCs show “peaked noise” or QPOs in the power-law section of the PDS. The QPOs, which may be related to the dynamic processes in the accretion disks, have received widespread attention. In this paper, however, we focus on the energy dependence of the overall PDS.

Several X-ray emission models of the GBHCs have suggested that the PDS should be energy dependent. Hua et al. (1997) have proposed that Comptonization in an extended hot, thermal corona may be responsible for the PDS shape and the hard time lags of GBHCs. Böttcher & Liang (1998) studied the pure Comptonization model in great detail for different source geometries. They assumed that the X-ray emission is generated by the upscattering of soft photons, which are injected from either a central or an external source. They showed that the Comptonization model with a central soft photon source generally has a steeper PDS at higher energies, but this steepening trend is less significant when the density gradient of the Comptonizing cloud increases. However, if the soft photon source is external, the steepening trend is less significant with lower density gradient. To avoid the unrealistic requirement of the pure Comptonization model for the huge size (e.g. $10^3 - 10^4 R_g$) of the Comptonizing corona, Böttcher & Liang (1999) proposed that the soft photons may be injected from a cool blob spiraling into the central object. In this scenario, the simulation shows that the PDS becomes flatter with increasing energies. In the magnetic flare model of Poutanen & Fabian (1999), a pulse-avalanche model is invoked in order to reproduce the overall shape of the observed PDS of Cygnus X-1. In this model, the general shape does not change with energy except that the second break frequency is shifted to lower frequencies for higher energy bands (Poutanen & Fabian 1999; J. Poutanen 1999, personal communication).

Given these different model predictions, it is important to find out in the available data how the PDS shape and integrated rms amplitude evolve with energy. The flattening PDS, as suggested by the spiraling blob model, was observed in Cygnus X-1 (Cui et al. 1997; Nowak et al. 1998). Smith & Liang (1999) reported that there were no significant PDS shape changes among the energy bands for an *RXTE* observation of GX 339-4, and that the rms amplitude decreased with increasing photon energy. GRS 1758-258, on the other hand, had the highest rms amplitude in the medium energy band (Lin et al. 1999). These different behaviors may be intrinsic to the sources, and thus different emission mechanisms or viewing geometries would be necessary for different GBHCs in spite of their spectral similarities. To address this issue, we have systematically analyzed the *RXTE* archival data for the four hard X-ray sources in their hard/low state: Cygnus X-1, GX 339-4, GRS 1758-258 and 1E 1740.7-2942. In section 2, we discuss how we select and reduce the data. In section 3, we show the analysis results. In section 4, we compare the results to various model predictions. In section 5, we discuss the results.

2. Data Selection and Reduction

The data have been properly selected from the *RXTE* archive over the period of 1996 – 1997. We chose only those data that came from long enough observations and had proper data formats

to allow us to do an accurate energy dependent analysis. In all cases, the sources were in the hard/low state, which was determined by careful spectral analyses. The dates of the observations are listed in Table 1. In order to study the energy dependence of the variability, we divided the PCA effective energy range into three energy bands, the ranges of which are approximately: 2 – 5 keV (L), 5 – 10 keV (M), and 10 – 40 keV (H). Some of the archival data formats make the energy ranges a little different from these values. The counts have been summed into time bins of 46.875 ms, and the power density spectra generated on intervals of 384 seconds. We subtracted from the data the background count rate estimated from the model L7/240 or (Q6+activation+X-ray). The contributions from the galactic diffuse emission, whose contamination to the X-ray flux of GRS 1758-258 and 1E 1740.7–2942 is significant, have also been subtracted from the light curves of the two sources, as described in Lin et al. (1999); see also Main et al (1999).

The power density spectrum for each band was generated using the FTOOLS analysis package with the white noise subtracted. For comparative purposes, we calculated the PDS over the frequency range of 0.002 – 10 Hz for all the sources even though some of them could be analyzed up to higher frequencies. We checked that we did not introduce any artificial effects by limiting the frequency range. For each observation, the final power density spectra have been averaged over all the observation segments. We calculated the H/L and M/L band ratios to investigate how the PDS shapes change with energy (the error of the PDS ratio is the propagating error). For each band we also integrated the PDS over the frequency range of 0.002 – 10 Hz, and took the square root to calculate the overall integrated rms amplitudes.

3. Analysis Results

3.1. Power Spectrum Shape

In Figure 1, we show an example of the energy dependent PDS and their ratios for one observation of Cygnus X-1. Similar results are seen in all seven observations of Cygnus X-1. The PDS ratios between the high- and low- energy bands significantly increase above 3 Hz. Below 3 Hz, the PDS ratios are consistent with constant values though there appears to be a slowly increasing trend. Moreover, we found that the two PDS ratios PDS_H/PDS_L and PDS_M/PDS_L start to increase roughly at the same frequency (3 Hz). Therefore, in terms of the double broken power law model, f_1 and f_2 are energy independent and β decreases with energy. The decrease in β means that the PDS shape becomes flatter at higher energies above f_2 . This flattening trend in Cygnus X-1 has been previously reported (van der Klis 1995; Cui et al. 1997; Nowak et al. 1998). The flat distribution of the PDS ratio over the frequency range between f_1 and f_2 indicates that the first power-law index, which is usually close to 1, indeed has little energy dependence.

No significant trends are seen for the other three sources. In all six observations of GX 339–4, we found the PDS ratios to be consistent with constants over the frequency range of 0.002 – 10 Hz (e.g. Figure 2), and we did not see any significant increases beyond 10 Hz either. Constant PDS

ratios mean that the PDS shapes are energy independent, and thus f_1 , f_2 and β of the double broken power law model have little energy dependence. Constant ratios were also found in all six observations of GRS 1758–258 (e.g. Figure 3) although detailed model fittings indicate that QPOs in the PDS are energy dependent (Lin et al. 1999). In three out of the five observations of 1E 1740.7–2942 the PDS ratios are also consistent with constants (e.g. Figure 4). In the other two observations of 1E 1740.7–2942, we found there were several big flares in the light curves. These flares, which have significant energy dependence, may be due to the nearby burst source previously detected by *RXTE* (Strohmayer et al. 1997). The burst source is located 0.8° away from the PCA pointing position. By excluding these flares from the timing analysis, we found the PDS ratios in these two observations are also consistent with a constant over 0.002 – 10 Hz. A complete analysis of the flares found in our 1997 Nov 11–12 observation of 1E 1740.7–2942 will be described in a separate paper (Lin et al. 2000) along with a full spectral analysis of 1E 1740.7–2942.

3.2. Overall Variability

The behaviors of the overall variability, represented by the integrated rms amplitude over the frequency range of 0.002 – 10 Hz, are significantly different among the four sources (Figure 5). 1E 1740.7–2942 has the lowest variability in the low energy band and has a general trend of increasing variability with energy except for the observation made in 1996 (MJD 50158), which has the highest variability in the medium band. GRS 1758–258 has the highest variability in the medium energy band and the lowest variability in the high band. GX 339–4 has a generally decreasing variability with increasing energy, except for two observations in which the medium energy band has slightly higher variability than the low band. Among the seven observations of Cygnus X–1, we found four cases with decreasing variability, one with constant variability and two with increasing variability, and the pattern appears to depend on the overall variability of the source.

Previously Cygnus X–1 and GX 339–4 have been reported to have little energy dependence (van der Klis 1995). This does not contradict our results. We have one observation of Cygnus X–1 (on MJD 50725) in which the overall variability is energy independent, and two other observations in which the integrated rms amplitude changes by less than 0.012 from the low to high energy bands. Similarly, in one observation of GX 339–4 (on MJD 50636), we see a change of less than 0.028 in the integrated rms amplitude over the three energy bands. Such small effects would have been indistinguishable in the early measurements (e.g. Nolan et al. 1981; Maejima et al. 1984).

When one considers that the spectra of the four sources are similar in the hard/low state, it seems surprising that the overall variability behaviors are so different. It is interesting to note that only one spectral property, the hydrogen column density due to the ISM and any materials local to the source is significantly different among the sources. The typical hydrogen column density for each source is shown in Figure 5. We see a tendency that the hydrogen column density anti-correlates with the variability of the source, especially in the low energy band. One possible

effect that the absorption has on the X-ray variation is that it might diminish the variability of the X-ray flux by absorbing and scattering the X-ray photons. 1E 1740.7–2942, for example, has the highest value for N_H , thus the diminishing effects on its X-ray flux can be significant up to 10 keV. This could make the lower two bands less variable if, for example, bright flares emitted from one region in the system are more absorbed than the general persistent emission.

By comparing the rms amplitudes with the related *RXTE* all sky monitor (ASM) (2 – 12 keV) count rates, we found a tendency towards an anti-correlation between the overall variability and the X-ray flux (Table 1 and Figure 6). Due to closeness of their values and the big statistical errors, the rms amplitudes and ASM count rates of the observations on MJD 50470 and 50517 for GRS 1758-258 have been combined, as have the observations on MJD 50158–61 and 50764 for 1E 1740.7-2942. This anti-correlation is consistent with previous timing results of Cygnus X–1, GX 339–4 and GS 2033+38 (van der Klis 1995; Nolan et al. 1981; Miyamoto et al. 1992), and can also be identified in the long-term monitoring of 1E 1740.7–2942 and GRS 1758–258 (see Figure 2 in Main et al. 1999). Again, this anti-correlation may imply that flaring and non-flaring emission regions are physically separated. With the increase of the non-flaring emission, the relative variation in the flux would decrease. We also compared the rms amplitude with the related BATSE Earth Occultation flux (20 – 120 keV), but no significant correlations were found.

4. Comparison with Aperiodic Variation Models

Since the discovery of rapid aperiodic X-ray intensity variations in Cygnus X–1 by Oda et al. (1971), various models of the aperiodic variations have been proposed. The early models were mostly phenomenological, such as shot models, but several more physical models have recently been proposed.

4.1. Shot Models

The shot models, originally proposed by Terrell (1972), are good at mimicking the observed light curves by superposing individual shots with properly chosen shot profiles. However, it is not clear how the shots are generated in the accretion disk (van der Klis 1995; Cui 1998). Takeuchi, Mineshige & Negor (1995) proposed a shot generation mechanism based on self-organized criticality (SOC). In the SOC model, the mass accretion takes place in the form of avalanches only when the local density exceeds some critical value. The model can produce the 1/f-like power density spectrum and predicts a positive correlation between the dissipated energy and the duration of the shot. The photon energy in each shot is determined by the local temperature of the disk where the shot is generated. Therefore, the SOC model alone does not make any predictions about the energy dependence of the PDS shape. Takeuchi & Mineshige (1997) further developed a more realistic SOC model to include the dynamic processes of advection-dominated accretion disks.

The viscosity parameter α is switched to a higher value when the surface density exceeds a critical value. Under this prescribed critical condition and the assumption of a uniform disk temperature, they showed that the improved SOC model can generate light curves and PDS similar to the observed ones. For a uniform temperature disk, the time profile of the thermal bremsstrahlung emissions is energy independent, and thus the PDS shape is also energy independent. To explain the energy dependent effects we have shown here, it will be necessary to expand this SOC model to the case of a multi-temperature disk. Such a multi-temperature disk is also needed to explain the X-ray energy spectra that have power-law photon indices higher than 1.

Like the SOC model, the wave propagation model (Manmoto et al. 1996) also needs an assumption for the temperature profile in the disk. The wave is generated by disturbances such as magnetic flares at the outer part of the disk and propagates into the event horizon without much damping. The wave model can account for the time profiles of individual X-ray shots, and predicts that the energy of the emitted photons increases as the wave propagates into the horizon because the local temperature of the disk increases with decreasing radius. This can explain the hard lags of the X-ray emission. The time profile of the X-ray flux in each energy band is determined by the velocity of the wave and the temperature profile of the disk. If the radial velocity is constant and the temperature distribution is linear along the radial direction, the time profiles of the shots are the same for all the energy bands, and then the PDS shape should be energy independent. This is consistent with our analysis results of GRS 1758–258, 1E 1740.7–2942, and GX 339–4. A more realistic version of the model will be required to explain the energy dependent behaviors of Cygnus X–1.

4.2. Comptonization Models

The hard-low state spectrum of GBHCs can best be interpreted as the unsaturated Comptonization of soft photons by hot thermal electrons (Katz 1976; Liang 1998). However, measurements of the Fourier-frequency dependence of the time lags between the signals in different X-ray energy channels indicates that this pure Comptonization model is not applicable to a moderate-sized uniform plasma (Miyamoto et al. 1988, 1993). Kazanas et al. (1997) and Hua et al. (1997) found that Comptonization in a hot, inhomogeneous corona with a density profile $n(r) \propto r^{-1}$ can fit the combined spectral and timing properties of Cygnus X-1, although the hot corona has to extend out to ~ 1 light second from the black hole. Böttcher & Liang (1998) studied the isolated effects of Comptonization on the rapid aperiodic variability of black hole X-ray binaries in great detail, investigating different source geometries. In the case of a central soft photon source, corresponding to an accretion-disk corona geometry with a covering fraction of the corona close to unity, the PDS was generally found to become steeper for increasing photon energies. This trend becomes weaker as the density gradient of the hot, thermal corona becomes steeper. If the soft photon source is external to the hot corona, which corresponds to an ADAF-like geometry (Narayan & Yi 1994; Chen et al. 1995; Esin, McClintock & Narayan 1997;

Luo & Liang 1998) with a cool outer accretion disk or a radiation-pressure dominated, hot inner accretion disk solution (Shapiro, Lightman & Eardley 1976), only a weak steepening of the PDS is predicted. This steepening trend is due to the averaging effect of Compton scatterings. Low energy photons, which have not gone through many up-scatterings, keep most of the variation of the soft photon input, while the high energy photons, having been accumulated in the corona for a longer time t , reflect the average of the soft photon input over a time t , and thus become less variable at high frequencies. For the same reason, the overall rms amplitude of the variability is expected to decrease with increasing photon energy. These predictions are not consistent with the data presented here. No cases of a steepening PDS shape were found. Therefore, the pure Compton scattering model does not fully explain the emission mechanism of GBHCs even for an inhomogeneous corona.

To overcome the problems with the pure Comptonization model, Böttcher & Liang (1999) developed a drifting blob model. It was motivated by the inhomogeneous accretion equilibrium found by Krolik (1998) and assumes that dense blobs of cool material are emitting soft photons and spiraling inward through a hot, optically thin inner accretion flow, which could be an ADAF or a Shapiro-Lightman-Eardley type hot inner disk. In this model, the hard time lags are due to the radial drifting time that the dense blobs spend in traveling from the cool to hot parts of the accretion flow. The model does not require a big Comptonization corona to account for the hard time lags, and thus the photon diffusion time is negligible. The photon flux resulting from a single drifting blob has significantly different time profiles in different energy bands. The low energy photon flux persists for the whole drifting period because most of the soft photons being steadily emitted by the drifting blob emerge from the corona without being upscattered to higher energy. On the other hand, most of the high energy photons emerge only at later times when the blob drifts to the inner hot part of the disk. Therefore, the high energy shots are much narrower than the low energy shots, and thus have a broader band in frequency space. Consequently, the PDS is predicted to become flatter with increasing photon energy. This is consistent with the observations of Cygnus X-1, which has flatter power spectra at higher energies. In order to reproduce the complete PDS of individual objects, additional assumptions about the production of these inward-drifting blobs are required. In the simplest picture, the overall rms amplitude of the variability is expected to increase with increasing photon energy. Since we have shown here that this is not always the case, a more detailed model may be required.

Another Compton scattering related model is the magnetic flare model proposed by Poutanen & Fabian (1999), which involves active regions of a patchy corona above an optically thick accretion disk. Driven by the hydrodynamic and radiation pressure, the active regions are moving away from the disk and being heated up by the magnetic energy. As the active regions move outward, they become hotter because there is less Compton cooling. The feedback radiation from the active regions also heats up the disk regions that provide the soft photons for the Compton scatterings in the active regions. These heating processes make the observed photon energy increase as the flares proceed, and thus the low energy photon flux reaches a maximum earlier

than the high energy flux. The light curves at different energies are self-similar but with higher characteristic time scales for higher energy photons. Consequently, the power density spectra in different energies have similar shapes with a energy independent β and a decreasing f_2 for higher energies. The first broken power law is determined by the avalanche processes, and thus it is energy independent. The PDS ratios would then decrease at frequencies above f_1 . However, we do not see this effect in any of our observations, implying that this version of the magnetic flare model is not supported.

5. Discussion

Our analysis shows that the classical black hole candidate Cygnus X–1 has significantly different temporal properties from 1E 1740.7–2942, GRS 1758–258 and GX 339–4 in spite of their similarities in energy spectra. The different energy dependence of the PDS shape may indicate that the emission mechanism in Cygnus X–1 is different from the other three GBHCs. If this is true, it will be necessary to develop accretion disk models that can accommodate this difference. The spiraling blob model, for example, could be the dominant mechanism for Cygnus X–1 while other mechanisms such as the wave propagation model may be more appropriate for the other three sources. However, these models do not exclude each other. Each of the models may just describe one aspect of the emission process. The SOC and wave models, for example, can be the blob generation mechanisms for the drifting blob model. Combining these models together will certainly make them more realistic and robust.

The analysis of the overall variability is complicated by the fact that the X-ray light curves may consist of two components: the shot component and the persistent component (Takeuchi & Mineshige 1997), which may have different origins and spectra. It is difficult to separate these two components spectrally and temporally. The integrated rms amplitude reflects total variability of the source emission and it is hard to directly compare the models that usually only simulate the shot processes. The SOC model is an exception. It generates shots using processes that occur in the steady accretion flow and, therefore, links the two components together. However, the energy dependence of the variability is still an open question for the SOC model.

The reason for the anti-correlating trend found between the integrated rms amplitude and the X-ray flux may also lie in the superposition of the shot and persistent components. If the radiation, for example, is dominated by the persistent component, any increase in the persistent flux would increase the total flux and thus reduce the relative variability, i.e., the integrated rms amplitude. If the emitting regions of the two components are physically separate, and there are locally more absorption materials around the shot emitting regions, then a high absorption would mean less variability. This would explain the anti-correlating trend between the rms amplitude and the hydrogen column density.

This work was supported by NASA grant NAG 5-3824 at Rice University. We thank Wei Cui and Juri Poutanen for their helpful discussions, David Smith for his assistance with the background determination for 1E 1740.7–2942 and GRS 1758–258, Jim Lochner and Gail Rohrbach of the *RXTE* team for their help with the data processing, and the anonymous referee for invaluable comments and suggestions. The work of M.B. is supported by NASA through Chandra Postdoctoral Fellowship Grant number PF9-10007 awarded by the Chandra X-ray Center, which is operated by the Smithsonian Astrophysical Observatory for NASA under contract NAS8-39073.

REFERENCES

- Balucińska-Church, M., Belloni, T., Church, M. J., & Hasinger, C. 1995, *A&A*, 302, L5
- Böttcher, M., & Liang, E. P. 1998, *ApJ*, 506, 281
- Böttcher, M., & Liang, E. P. 1999, *ApJ*, 511, L37
- Chen, X., Abramowicz, M. A., Lasota, J.-P., Narayan, R., & Yi, I. 1995, *ApJ*, 443, L61
- Cui, W., Zhang, S. N., Focke, W., & Swank, J. H. 1997, *ApJ*, 484, 383
- Cui, W. 1998, in “High-Energy Processes in Accreting Black Holes”, eds. J. Poutanen & R. Svensson, *ASP Conf. Series*, Vol. 161, p. 97
- Esin, A. E., McClintock, J. E., & Narayan, R. 1997, *ApJ*, 489, 865
- Hua, X.-M., Kazanas, D., & Titarchuk, L. 1997, *ApJ*, 482, L57
- Katz, J. I. 1976, *ApJ*, 206, 910
- Kazanas, D., Hua, X.-M., & Titarchuk, L. 1997, *ApJ*, 480, 735
- Krolik, J. H. 1998, *ApJ*, 498, L13
- Liang, E. 1998, *Phys. Rep.*, 302, 67
- Lin, D., Smith I. A., Liang, E. P., Bridgman, T., Smith, D. M., Martí, J., Durouchoux, Ph., Mirabel, I. F., & Rodríguez, L. F. 1999, *ApJ*, submitted
- Lin, D., Smith I. A., Liang, E. P., Böttcher, M. 2000, in preparation
- Luo, C., & Liang, E. P. 1998, *ApJ*, 498, 307
- Maejima, Y., Makishima, K., Matsuoka, M., Ogawara, Y., Oda, M., Tawara, Y., & Doi, K. 1984, *ApJ*, 285, 712
- Main, D. S., Smith D. M., Heindl W. A., Swank J., Leventhal M., Mirabel, I. F., Rodríguez, L. F. 1999, to appear in *ApJ*, astro-ph/9906178
- Manmoto, T., Takeuchi, M., Mineshige, S., Matsumoto, R., & Negoro, H. 1996, *ApJ*, 464, L135
- Méndez, M., & Van der Klis, M. 1997, *ApJ*, 479, 926
- Miyamoto, S., Kitamoto, S., Mitsuda, K., & Dotani, T. 1988, *Nature*, 336, 450
- Miyamoto, S., Kitamoto, S., Iga, S., Negoro, H., & Terada, K. 1992, *ApJ*, 391, L21
- Miyamoto, S., Iga, S., Kitamoto, S., & Kamado, Y. 1993, *ApJ*, 403, L39

- Narayan, R., & Yi, I. 1994, ApJ, 428, L13
- Nolan, P. L., et al. 1981, ApJ, 246, 494
- Nowak, M. A., Vaughan, B. A., Wilms, J., Dove, J. B., & Begelman, M. C. 1998, ApJ, 510, 874
- Oda, M., Gorenstein, P., Gursky, H., Kellogg, E., Schreier, E., Tananbaum, H., & Giacconi, R. 1971, ApJ, 166, L1
- Poutanen, J., & Fabian, A. C. 1999, MNRAS, 306, L31
- Shapiro, S., Lightman, A. P., & Eardley, D. M. 1976, ApJ, 204, 187
- Sheth, S., Liang, E., Lou, C., & Murakami, T. 1996, ApJ, 468, 755
- Smith, I. A., & Liang, E. P. 1999, ApJ, 519, 771
- Strohmayer, T. E., Jahoda, K., Giles, A. B., & Lee, U. 1997, ApJ, 486, 355
- Takeuchi, M., Mineshige, S., & Negoro, H. 1995, PASJ, 47, 617
- Takeuchi, M., & Mineshige, S. 1997, ApJ, 486, 160
- Terrell, N. J. 1972, ApJ, 174, L35
- van der Klis, M. 1995, in X-Ray Binaries (Cambridge: Cambridge Univ. Press)

Table 1. The observation date of each curve in Figure 5 and its related *RXTE* ASM (2 – 12 keV) daily count rate.

# ^a	Cyg X–1		GX 339–4		GRS 1758–258		1E 1740.7–2942	
	Date ^b	ASM ^c	Date ^b	ASM ^c	Date ^b	ASM ^c	Date ^b	ASM ^c
1	465	19.7 ± 0.7	636	1.4 ± 0.5	646	1.4 ± 0.5	504	1.7 ± 0.4
2	467	17.7 ± 0.4	749	1.4 ± 0.7	673/74/78 /80/84	1.7 ± 0.5	158–61	2.9 ± 0.6
3	725	26.0 ± 0.4	597	1.7 ± 0.5	562	1.7 ± 0.4	764	2.8 ± 1.5
4	128	34.3*	711	4.0 ± 0.5	513	3.1 ± 0.8	763	2.1*
5	125	33.8*	482	3.1 ± 0.8	470	7.6 ± 2.0	584–88	2.4 ± 0.3
6	130	34.6*	553	5.5 ± 0.3	517	6.3 ± 1.3		
7	624	30.0 ± 0.4						

^aThe curve number (the first column) is counted from top to bottom in the medium energy band (5 – 10 keV) in Figure 5; thus the rms amplitudes are in the decreasing order for each source.

^bThe date is the Modified Julian Date – 50000.

^cThe count rate is in counts/s, and the count rates superscribed by ‘*’ are interpolated from the measurements before and after the observation date.

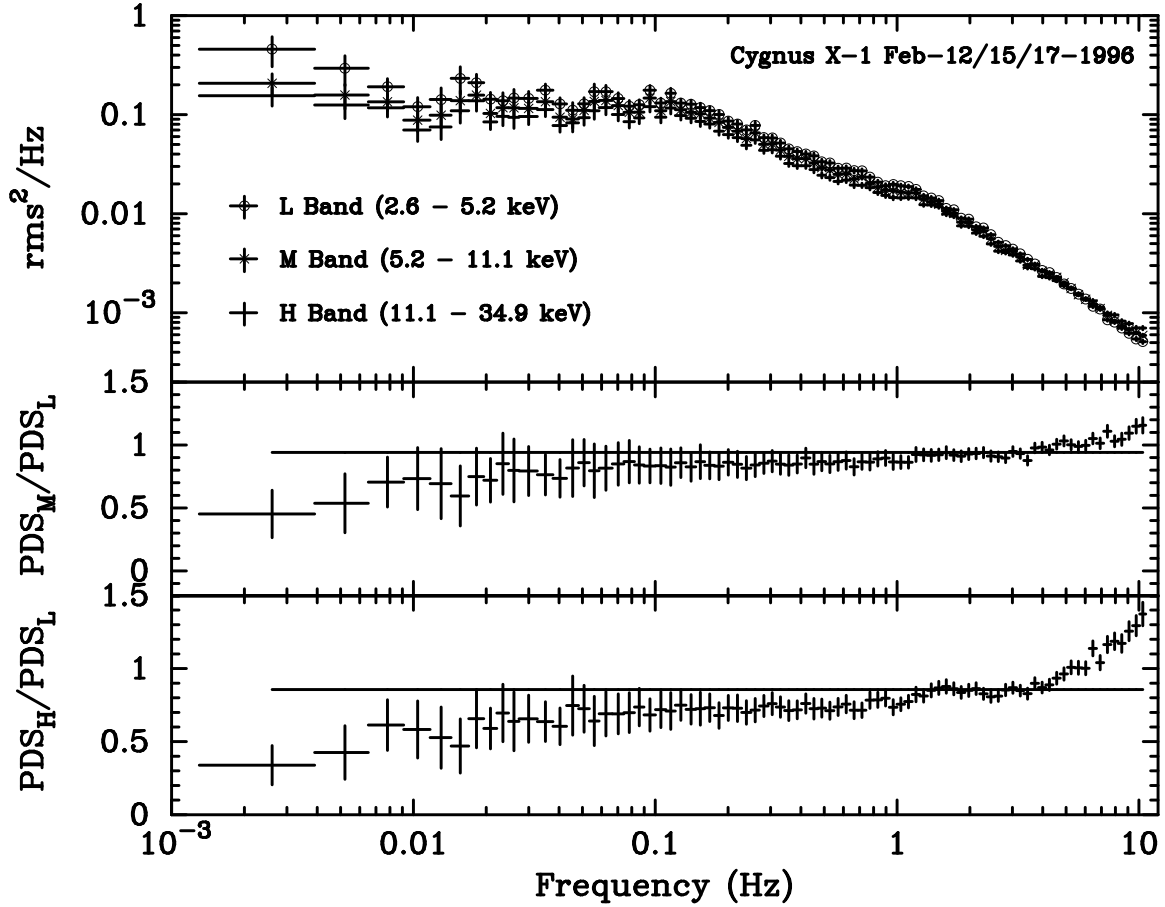


Fig. 1.— A sample PDS of Cygnus X-1 and the PDS ratios between the energy bands. The upper panel is the PDS for the three energy bands. The lower two panels are the PDS ratios between the L band and the other two bands. Constant fits to the PDS ratios over the whole frequency range give a $\chi^2_\nu = 1.85$ for 82 degrees of freedom (DOF) and null hypothesis probability $Q = 4.47 \times 10^{-6}$ for $\text{PDS}_M/\text{PDS}_L$ and a $\chi^2_\nu = 5.6$ (DOF = 82) and $Q = 7.2 \times 10^{-54}$ for $\text{PDS}_H/\text{PDS}_L$. The increasing PDS ratio indicates a flatter power spectrum at higher energies.

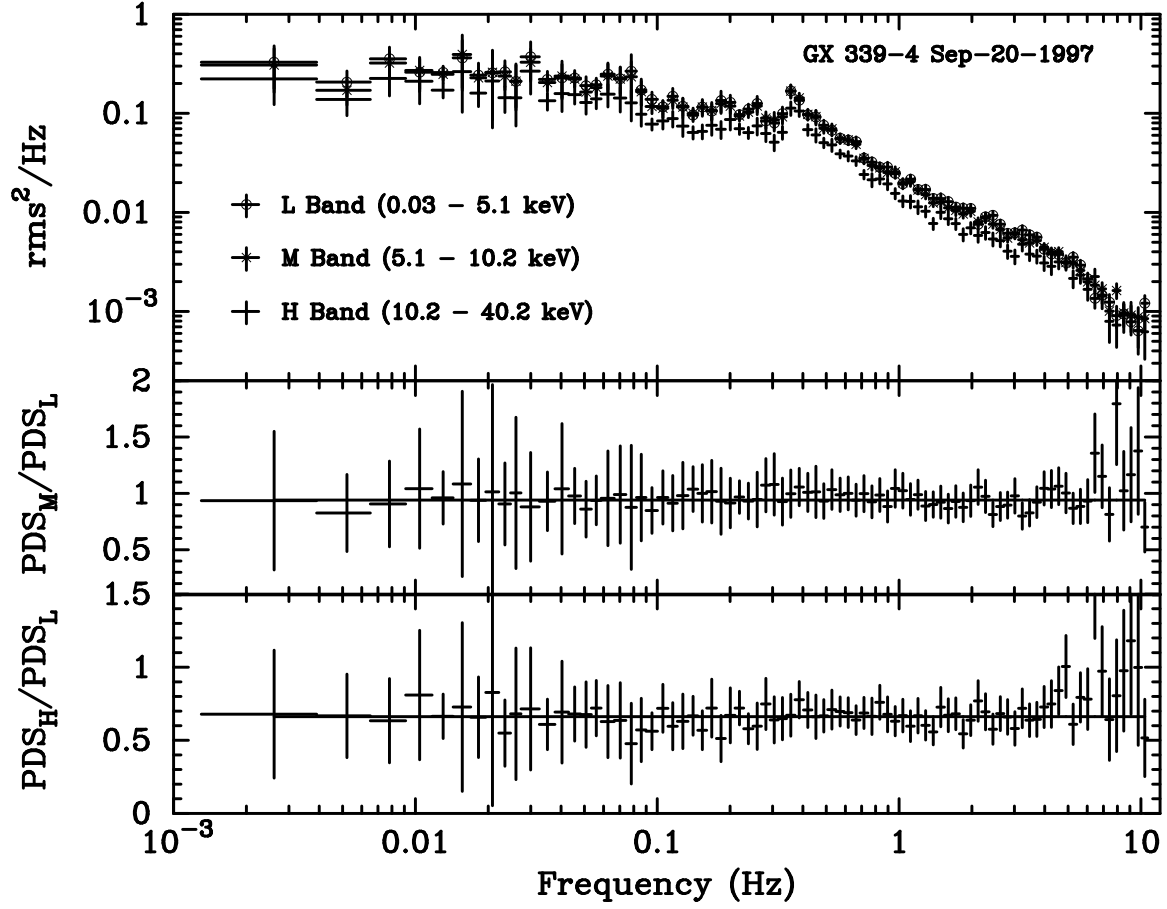


Fig. 2.— A sample PDS of GX 339-4 and the PDS ratios between the energy bands. Constant fits to the PDS ratios over the whole frequency range give a $\chi^2_\nu = 0.23$ (DOF = 82) and $Q \approx 1.0$ for $\text{PDS}_M/\text{PDS}_L$ and a $\chi^2_\nu = 0.41$ (DOF = 82) and $Q \approx 1.0$ for $\text{PDS}_H/\text{PDS}_L$. The flat PDS ratio indicates an energy independent shape of the power spectrum.

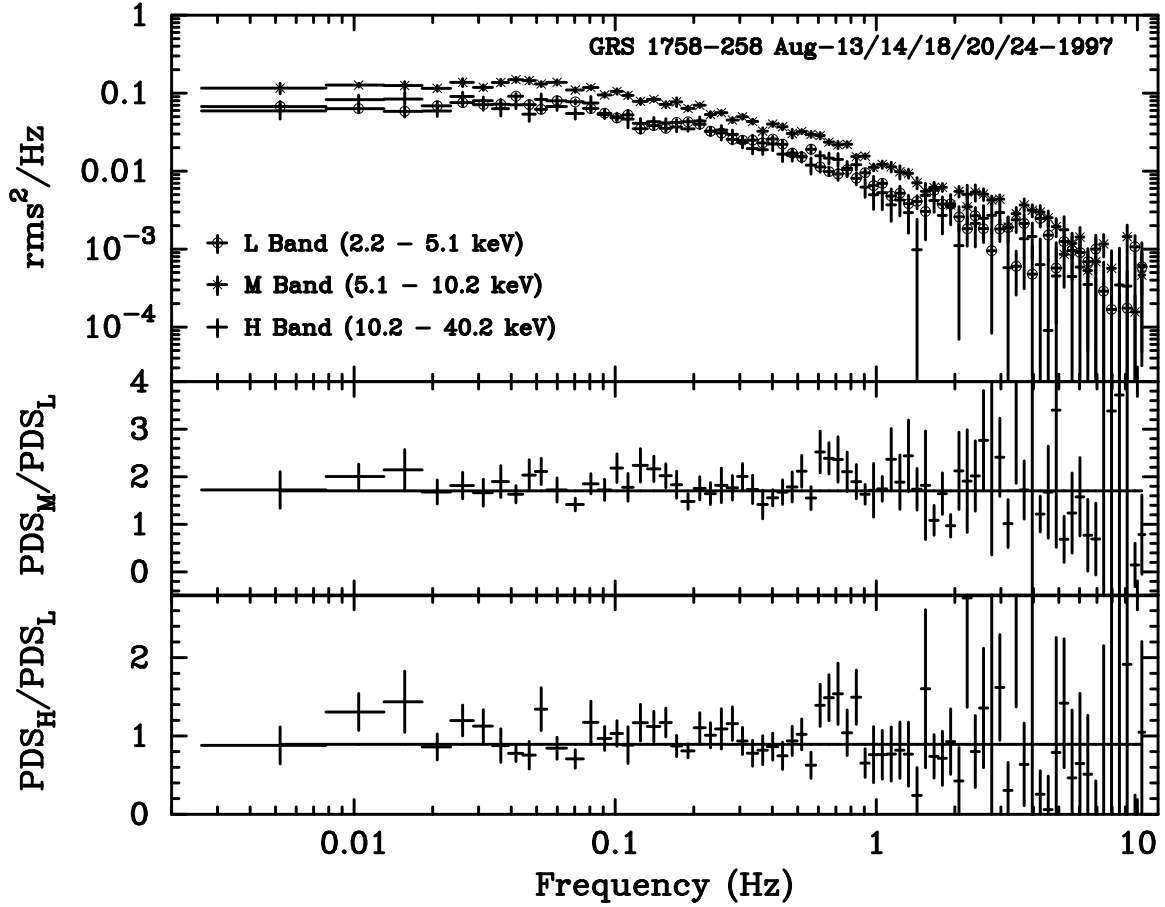


Fig. 3.— A sample PDS of GRS 1758-258 and the PDS ratios between the energy bands. Constant fits to the PDS ratios over the whole frequency range give a $\chi^2_\nu = 1.17$ (DOF = 72) and $Q = 0.15$ for $\text{PDS}_M/\text{PDS}_L$ and a $\chi^2_\nu = 0.41$ (DOF = 72) and $Q = 0.24$ for $\text{PDS}_H/\text{PDS}_L$.

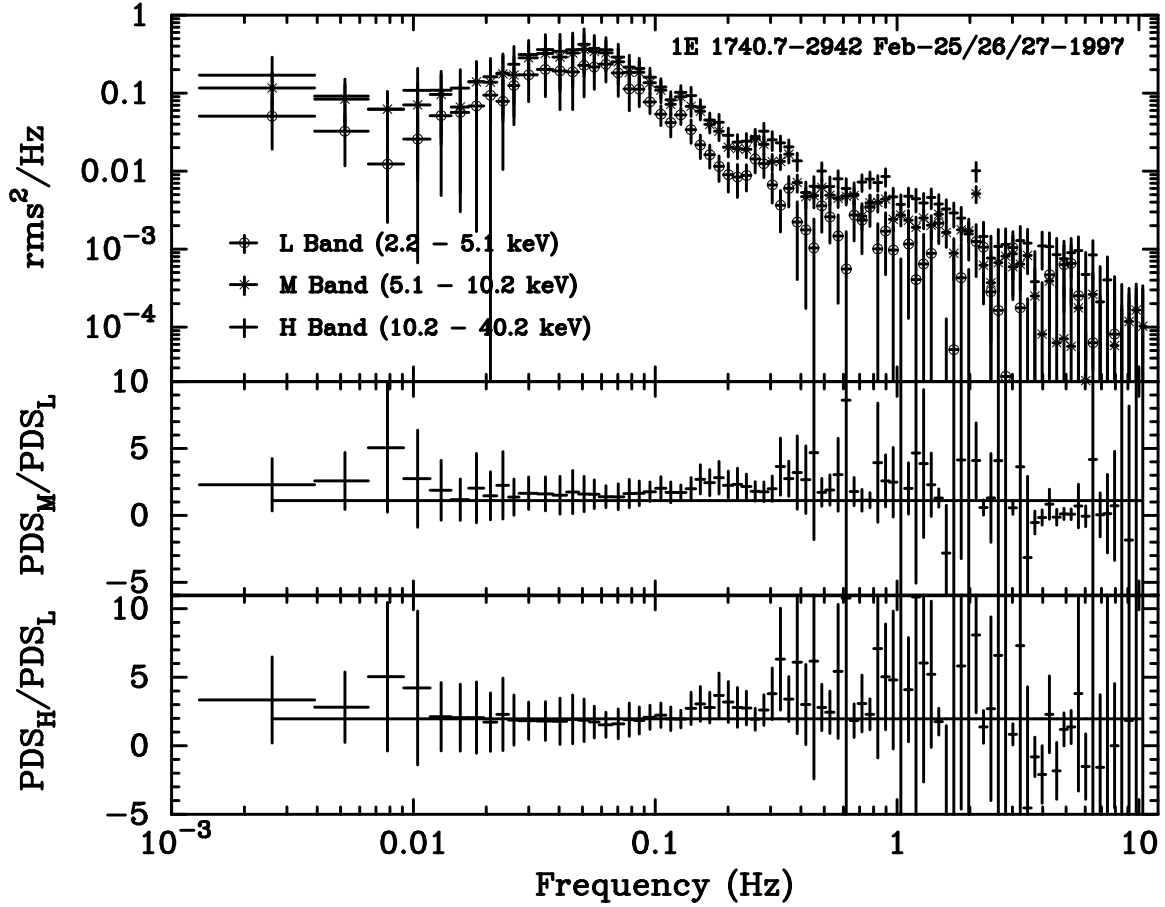


Fig. 4.— A sample PDS of 1E 1740.7-2942 and the PDS ratios between the energy bands. Constant fits to the PDS ratios over the whole frequency range give a $\chi^2_\nu = 0.94$ (DOF = 82) and $Q = 0.76$ for $\text{PDS}_M/\text{PDS}_L$ and a $\chi^2_\nu = 0.41$ (DOF = 82) and $Q \approx 1.0$ for $\text{PDS}_H/\text{PDS}_L$.

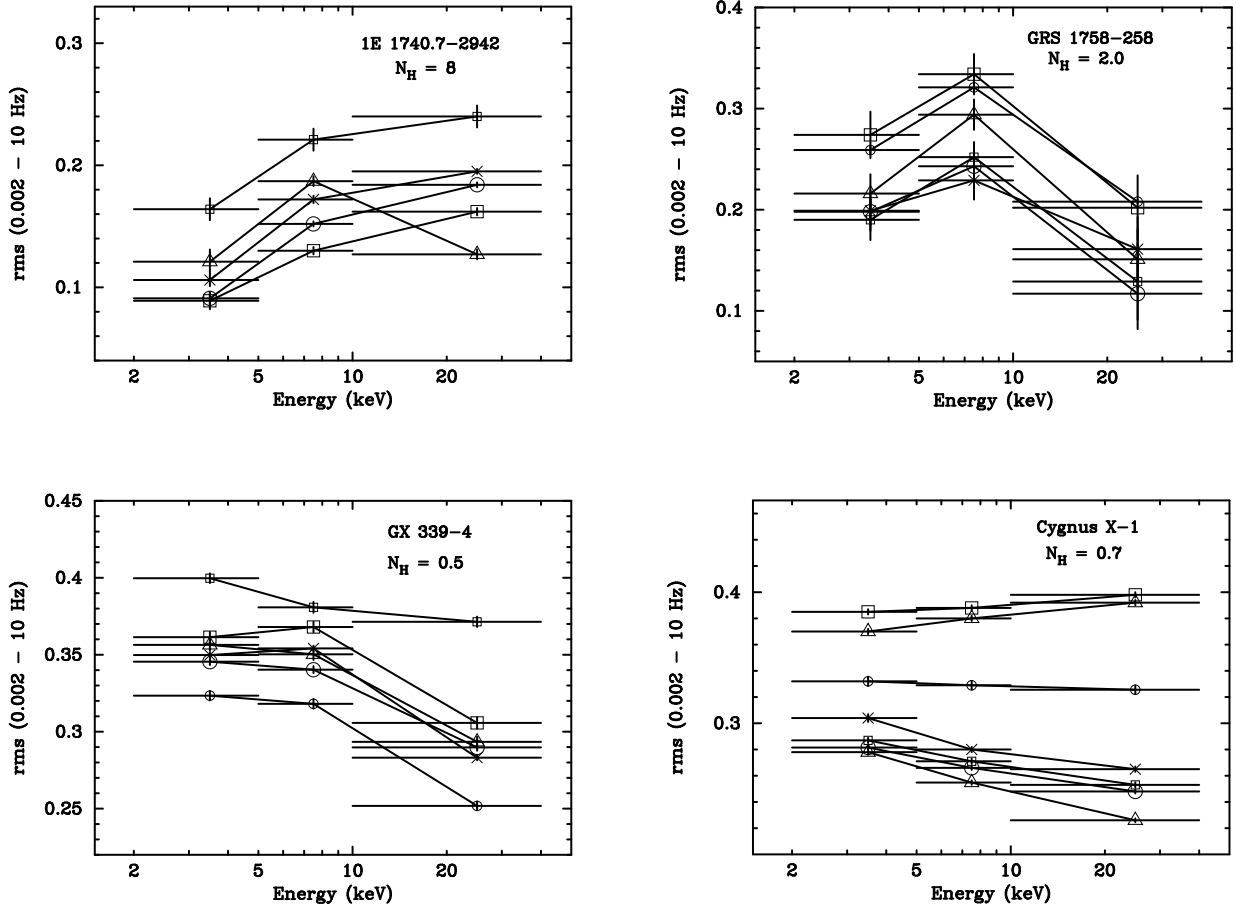


Fig. 5.— The overall variability vs energy. The rms is calculated by integrating the PDS over the frequency range of 0.002 – 10 Hz and taking the square root of the integral. Each connected curve represents one observation with the corresponding dates and the related ASM daily count rates listed in Table 1. N_H gives the typical hydrogen column density measured for the four sources in units of 10^{22} cm^{-2} (1E 1740.7-2942: Sheth et al. 1996; GRS 1758-258: Lin et al. 1999; GX 339-4: Méndez & Van der Klis 1997; Cyg X-1: Balucińska-Church et al. 1995). The energy dependence of the overall variability is significantly different among the four sources.

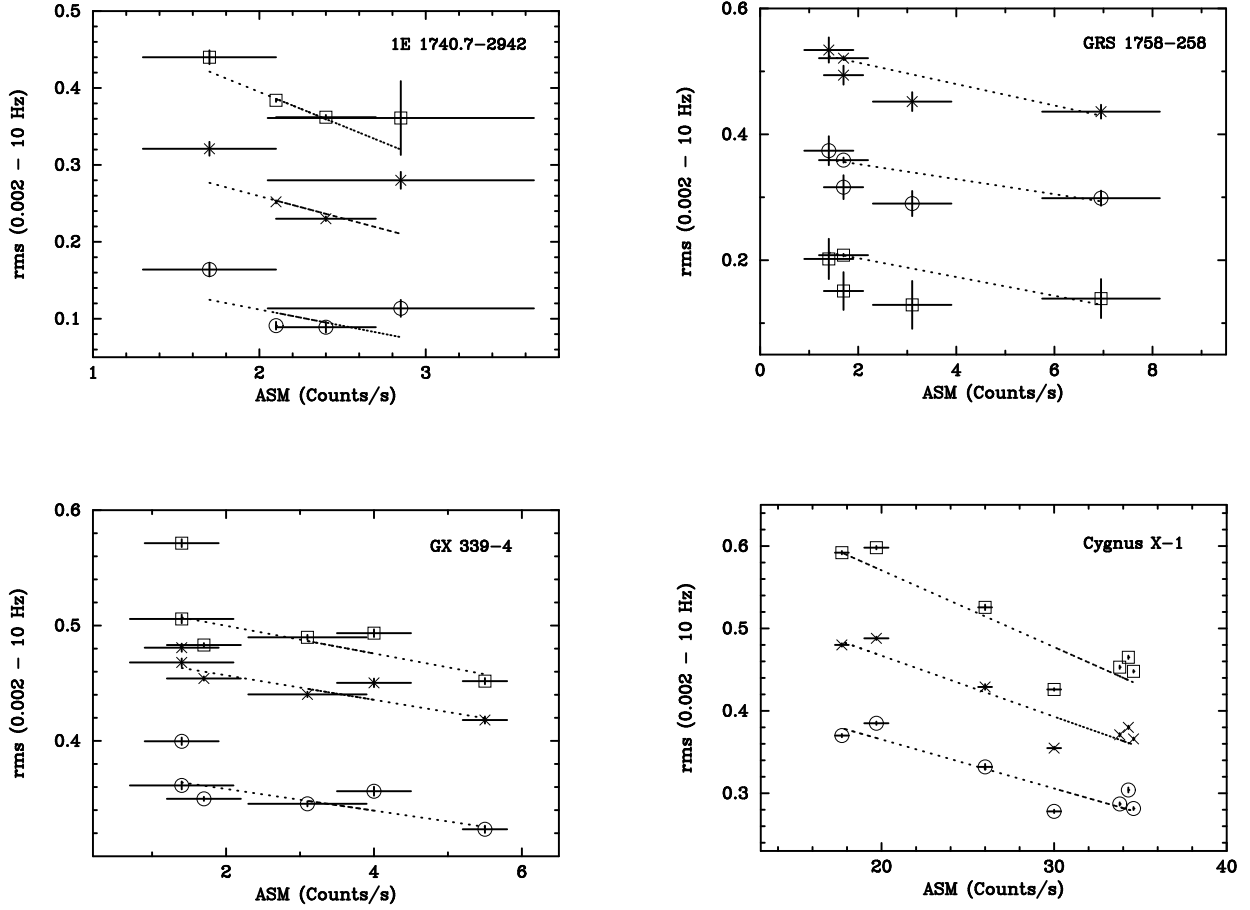


Fig. 6.— The anti-correlation between the integrated rms amplitude and count rate of *RXTE* ASM (2 – 12 keV). For illustrative purposes, the rms amplitudes for band M (crosses) have been shifted upwards by 0.1, and band H (squares) by 0.2 except for GRS 1758-258, whose rms amplitude in band H has been shifted upwards by 0.3. No shifts have been made to band L (circles). The dotted lines are the best fit linear functions for each data set.